The Astrophysical Journal Letters, 910:L11 (7pp), 2021 March 20 https://doi.org/10.3847/2041-8213/abed58

Pure Density Evolution of the Ultraviolet Quasar Luminosity Function at $2 \lesssim z \lesssim 6$

Yongjung Kim[1,2,4] and Myungshin Im[2,3]
[1] Kavli Institute for Astronomy and Astrophysics, Peking University, Beijing 100871, People's Republic of China; yongjungkim@pku.edu.cn
[2] SNU Astronomy Research Center, Seoul National University, 1 Gwanak-ro, Gwanak-gu, Seoul 08826, Republic of Korea; mim@astro.snu.ac.kr
[3] Astronomy Program, Department of Physics & Astronomy, Seoul National University, 1 Gwanak-ro, Gwanak-gu, Seoul 08826, Republic of Korea
Received 2021 February 7; revised 2021 March 8; accepted 2021 March 10; published 2021 March 23

Abstract

The quasar luminosity function (QLF) shows the active galactic nucleus (AGN) demography as a result of the combination of the growth and the evolution of black holes, galaxies, and dark matter halos along the cosmic time. The recent wide and deep surveys have improved the census of high-redshift quasars, making it possible to construct reliable ultraviolet (UV) QLFs at $2 \lesssim z \lesssim 6$ down to $M_{1450} = -23$ mag. By parameterizing these up-to-date observed UV QLFs that are the most extensive in both luminosity and survey area coverage at a given redshift, we show that the UV QLF has a universal shape and its evolution can be approximated by a pure density evolution (PDE). In order to explain the observed QLF, we construct a model QLF employing the halo mass function, a number of empirical scaling relations, and the Eddington ratio distribution. We also include the outshining of AGN over its host galaxy, which made it possible to reproduce a moderately flat shape of the faint end of the observed QLF (slope of ~ -1.1). This model successfully explains the observed PDE behavior of UV QLF at $z > 2$, meaning that the QLF evolution at high redshift can be understood under the framework of halo mass function evolution. The importance of the outshining effect in our model also implies that there could be a hidden population of faint AGNs ($M_{1450} \gtrsim -24$ mag), which are buried under their host galaxy light.

Unified Astronomy Thesaurus concepts: Quasars (1319); Active galactic nuclei (16); Luminosity function (942); Supermassive black holes (1663)

1. Introduction

As an observable black hole (BH) over a wide redshift range, quasars, the most powerful active galactic nuclei (AGNs), have been playing a pivotal role in understanding the formation and the growth of BH along the cosmic time. The quasar demography at a given redshift, represented by the quasar luminosity function (QLF), is the result of intertwining evolution of several physical properties of BHs and their host galaxies: the gas fueling mechanism, the obscuration of quasars by dust, the growth of quasar host galaxies/halos, to name a few. Therefore, by studying the cosmic evolution of QLF, one can comprehend a general picture of how halos, galaxies, and BHs evolved together.

The observed QLFs have been examined in various ways. Hopkins et al. (2007) and Shen et al. (2020) assembled a large number of observed QLFs and determined the bolometric QLF as a function of redshift. Similarly, Manti et al. (2016) and Kulkarni et al. (2019) also parameterized the ultraviolet (UV) QLF, using available data at that time. Other studies focused on the determination of QLF from the empirically/observationally constrained relations among quasars, galaxies, and dark matter halos, by using the conditional luminosity function (Conroy & White 2013; Ren et al. 2020) or continuity equation (Tucci & Volonteri 2017). Veale et al. (2014) also presented simple models with the growth-based evolution of BHs and galaxies. These studies show that the QLF evolution at $z \lesssim 3$ is complicated, favoring an interwoven evolution of the number density, the luminosity, and the bright/faint-end slopes.

At $z > 3$, however, the QLF studies had been fundamentally hampered by the lack of faint quasars that can define the QLF faint-end slope. For example, the Sloan Digital Sky Survey (SDSS) discovered quasars up to $z \sim 6$, but the SDSS high-redshift quasar sample is limited to the brightest ones with the absolute magnitude at 1450 Å of $M_{1450} < -25$ mag (Jiang et al. 2016). With bright quasars alone, the previous studies were limited to constraining the bright-end slope of QLFs (Hopkins et al. 2007; Conroy & White 2013; Veale et al. 2014). Very recently, subsequent large-area imaging surveys expanded the luminosity range of the $z \gtrsim 4$ quasar sample down to $M_{1450} = -23$ mag or fainter (Akiyama et al. 2018; Matsuoka et al. 2018; McGreer et al. 2018; Kim et al. 2019, 2020; Niida et al. 2020). Using a sample of dozens or more faint quasars, one can now obtain a meaningful constraint on the faint end of UV QLF.

In this Letter, we investigate the evolution of QLF at $2 \lesssim z \lesssim 6$ using the most up-to-date observed QLFs. We show that the UV QLF evolution is dominated by a pure density evolution (PDE) and provide possible interpretations for this rather unexpected result. The cosmological parameters we adopted are $\Omega_m = 0.3$, $\Omega_\Lambda = 0.7$, and $H_0 = 70$ km s^{-1} Mpc^{-1}.

2. Observed UV QLF

The first step to figuring out the evolutionary trend of quasar demography is to select the QLFs that are least biased at their faint ends. Among dozens of UV QLFs at $2 \lesssim z \lesssim 6$ in the literature, we first collect the QLFs based on the quasars selected by their unique rest-UV colors, rather than by X-ray detection (e.g., Giallongo et al. 2019) or photometric variability (e.g., Palanque-Delabrouille et al. 2016). Then, we excluded the QLFs derived from the quasar sample from a small survey area (<10 deg^2) or consisting of only bright ones ($M_{1450} < -24$ mag). If there are several results at a given redshift, we chose the one that used the largest number of

[4] KIAA Fellow.

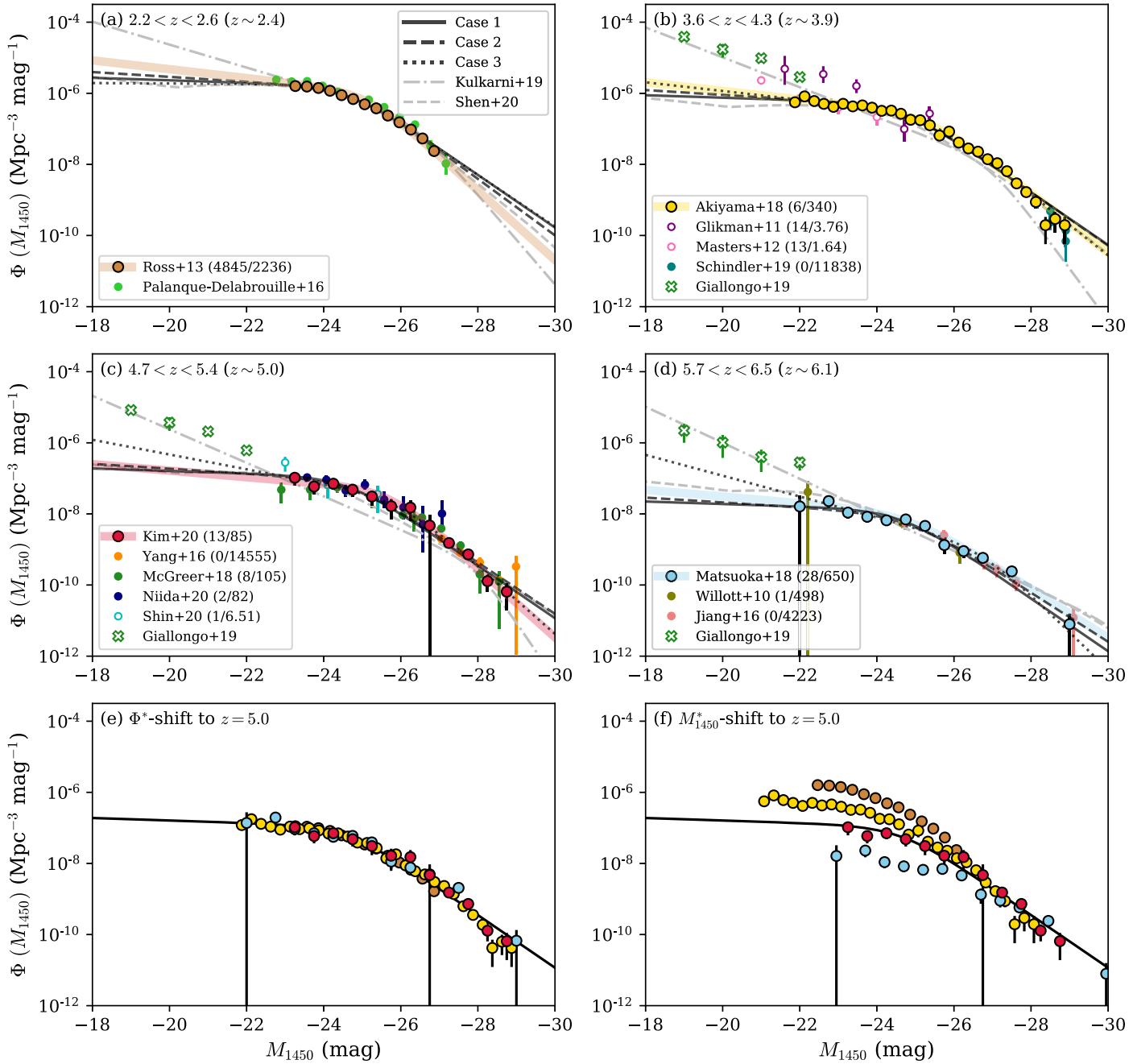

Figure 1. Panels (a)–(d): observed QLFs at $2 \lesssim z \lesssim 6$. The redshift range and the central redshift are marked in each panel. The filled (open) circles denote the QLFs from the large (small) area surveys. The numbers in the parentheses in the legend represent the number of spectroscopically identified quasars at $M_{1450} > -24$ mag ($N_{\rm spec,-24}$) and the survey area in deg^2 of each study, i.e., ($N_{\rm spec,-24}$/Area). The QLFs selected for this study are highlighted by the black circles (Ross et al. 2013; Akiyama et al. 2018; Matsuoka et al. 2018; Kim et al. 2020) with their parametric QLFs (thick translucent line). The green open crosses are from the X-ray-selected quasar sample (Giallongo et al. 2019). The black solid, dashed, and dotted lines denote the best-fit QLF in cases 1, 2, and 3, respectively. The empirical models of Kulkarni et al. (2019) and Shen et al. (2020) are shown as the gray dotted–dashed and dashed lines, respectively. Panels (e)–(f): shifted QLFs by scaling Φ^* or M^*_{1450} to fit to the faint end and bright end of the $z \sim 5$ QLF, respectively. The solid line represents the best-fit $z \sim 5$ result in case 1.

spectroscopically identified quasars at $M_{1450} > -24$ mag ($N_{\rm spec,-24}$). For example, at $z \sim 5$, there are three comparable studies: McGreer et al. (2018; 105 deg^2), Kim et al. (2020; 85 deg^2), and Niida et al. (2020; 82 deg^2). But their $N_{\rm spec,-24}$ are 8, 13, and 2, respectively, so we took the result of Kim et al. (2020).

Figure 1 shows the selected QLFs (marked with black circles) at four different redshift bins (Ross et al. 2013; Akiyama et al. 2018; Matsuoka et al. 2018; Kim et al. 2020) of which central redshifts are $z \sim 2.4$, 3.9, 5.0, and 6.1. These QLFs are shifted in absolute magnitudes and number densities to our chosen cosmological parameters. For the Ross et al. (2013) QLF at $z \sim 2.4$, their $M_i(z = 2)$ magnitudes are converted to M_{1450} following the prescription in Appendix B of their work. Akiyama et al. (2018) used the photometric redshift sample with only $N_{\rm spec,-24} = 6$. However, their photometric redshift accuracy is small enough ($\Delta z/(1+z) \sim 0.03$) to accurately trace the LF shape. We note that the bright ends ($M_{1450} \lesssim -27$) of the three selected QLFs (Akiyama et al. 2018; Matsuoka et al. 2018; Kim et al. 2020) are determined by the bright quasar sample from other studies (e.g., SDSS). As a result, the selected QLFs

cover wide ranges in luminosity ($-30 < M_{1450} < -23$) and survey area (>80 deg^2), and can be considered the best-determined QLF to date.

In Figure 1, we compare QLFs from different literature. After homogenizing the cosmological parameters to our chosen values, QLFs are shifted in number density to the central redshift of the selected QLFs within each redshift panel, with the number density scaling factor we present in this work (case 1 in Section 3). The selected QLFs are in good agreement with the other QLFs based on large-area survey data (filled circles; Willott et al. 2010; Jiang et al. 2016; Palanque-Delabrouille et al. 2016; Yang et al. 2016; McGreer et al. 2018; Schindler et al. 2019; Niida et al. 2020), although some QLFs from small area surveys (<10 deg^2) tend to deviate from the selected ones (open circles and crosses; Glikman et al. 2011; Masters et al. 2012; Giallongo et al. 2019; Shin et al. 2020).

The thick translucent lines in Figure 1 denote the parametric QLF ($\Phi_{\rm par}$), canonically described by a double power-law (DPL) function:

$$\Phi_{\rm par}(M_{1450}, z) = \frac{\Phi^*}{10^{0.4(\alpha+1)(M_{1450}-M^*_{1450})} + 10^{0.4(\beta+1)(M_{1450}-M^*_{1450})}}, \quad (1)$$

where Φ^* is the normalization factor, M^*_{1450} is the break magnitude, and α and β are the faint- and bright-end slopes, respectively. The best-fit parameters are taken from the corresponding references (Ross et al. 2013; Akiyama et al. 2018; Matsuoka et al. 2018; Kim et al. 2020).

The striking feature in Figure 1 is the similarity of the shape of QLFs at different redshifts. In panels (e) and (f), we show QLFs shifted only in density and only in luminosity, respectively. We note that the density-shift alone makes the QLFs overlap almost perfectly with each other.

3. Redshift Evolution of QLF

To describe the redshift evolution, we assume polynomial functions for the four parameters of $\Phi_{\rm par}$:

$$X(z) = \sum_{i=0}^{n_X} C_{X,i}\,(z - z_p)^i, \quad (2)$$

where $X \in \{\log_{10}\Phi^*, M_{1450}, \alpha, \beta\}$, $C_{X,i}$ is the i-th order coefficient for the parameter X, n_X is the maximum order, and $z_p = 2.2$ (pivot redshift). Here we consider three cases:

1. Case 1: a PDE model where only Φ^* evolves, and to the second order, i.e., $n_X \in \{2, 0, 0, 0\}$ for X.
2. Case 2: in addition to the number density evolution of Case 1, we allow the bright-end slope β to evolve but to the first order (see Figure 1), i.e., $n_X \in \{2, 0, 0, 1\}$ for X.
3. Case 3: in addition to the number density evolution of Case 1, we allow all the other parameters to evolve but to the first order, i.e., $n_X \in \{2, 1, 1, 1\}$ for X.

We fit these functions to the observed QLF data points ($\Phi_{\rm obs}$), with the maximum likelihood estimation. For this, we used the `emcee` Python package[5] (Foreman-Mackey et al. 2013) for the Markov Chain Monte Carlo sampling of the DPL parameters. We used a likelihood function of $\mathcal{L} = -\frac{1}{2}\sum[(\Phi_{\rm obs} - \Phi_{\rm par})/\sigma_{\Phi_{\rm obs}}]^2$, where $\sigma_{\Phi_{\rm obs}}$ is the 1σ uncertainty of $\Phi_{\rm obs}$ from the literature. We used uninformative priors on the parameters within the reasonable ranges: $-10 < \log_{10}\Phi^* < 0$, $-30 < M^*_{1450} < -23$, $-5 < \alpha, \beta < 0$, and $-1 < C_{X,i} < 1$. The best-fit results with 1σ errors are taken to be the median values with standard deviations of their posterior distributions with 10,000 chains, listed in Table 1.

Table 1
Best-fit DPL Parameters

X	$C_{X,0}$	$C_{X,1}$	$C_{X,2}$
	Case 1		
$\log_{10}\Phi^*$	-5.77 ± 0.03	-0.12 ± 0.02	-0.11 ± 0.01
M^*_{1450}	-24.64 ± 0.07	⋯	⋯
α	-1.09 ± 0.04	⋯	⋯
β	-2.86 ± 0.03	⋯	⋯
	Case 2		
$\log_{10}\Phi^*$	-5.83 ± 0.03	-0.13 ± 0.02	-0.11 ± 0.01
M^*_{1450}	-24.82 ± 0.08	⋯	⋯
α	-1.17 ± 0.04	⋯	⋯
β	-3.01 ± 0.05	0.07 ± 0.02	⋯
	Case 3		
$\log_{10}\Phi^*$	-5.68 ± 0.04	-0.32 ± 0.03	-0.13 ± 0.01
M^*_{1450}	-24.40 ± 0.11	-0.59 ± 0.09	⋯
α	-0.98 ± 0.07	-0.19 ± 0.04	⋯
β	-2.78 ± 0.06	-0.22 ± 0.05	⋯

Note. Φ^* is in units of Mpc^{-3} mag^{-1}.

The resultant QLFs are shown in Figure 1 with the solid, dashed, and dotted lines. They are consistent with each other, supported by the fact that the residuals ($\Delta\Phi = \log_{10}\Phi_{\rm obs} - \log_{10}\Phi_{\rm par}$) for the selected QLFs have the normal-like distributions with a standard deviation of only 0.15 to 0.12 dex from cases 1 to 3. We note that the reduced chi-square (χ^2_ν) value between the best-fit result and observation naturally decreases as the model becomes complicated with the increasing number of free parameters, but only mildly; $\chi^2_\nu = 3.14$, 2.93, and 2.22 from cases 1 to 3.

In Figure 2, we show the changes in parameters of our models along the redshift with the best-fit parameters of $\Phi_{\rm par}$ in the literature. Note that we only plot the results determined from the maximum-likelihood method to individual quasars (not to the binned QLFs). Our results are broadly consistent with the parameters of the observed QLFs selected for the study. Unlike cases 1 and 2, there are large discrepancies between the case 3 fit and the local best-fit values at $z \sim 6$, although the largest number of free parameters were used in case 3. This is due to the high dependence of our MCMC run on the lower-redshift QLFs (Ross et al. 2013; Akiyama et al. 2018) that have a larger number of data points with smaller uncertainties than the high-redshift QLFs. The case 3 result is the best mathematically, but we point out that it is only slightly more accurate than others in terms of $\Delta\Phi$ and χ^2_ν.

There are several QLF parameters in disagreement (Yang et al. 2016; Kulkarni et al. 2019; Schindler et al. 2019; Niida et al. 2020). In the case of Niida et al. (2020), their main result with a fixed slope of $\beta = -2.9$ (navy triangles) always shows higher values in all the parameters than those without any fixed parameters (navy circles). This implies that the correlation between QLF parameters may show up as mathematical difference (e.g., see Matsuoka et al. 2018; Kim et al. 2020). Also, the results biased toward lower values than our models (Yang et al. 2016; Kulkarni et al. 2019; Schindler et al. 2019) can be attributed to the use of

[5] https://emcee.readthedocs.io/en/stable/

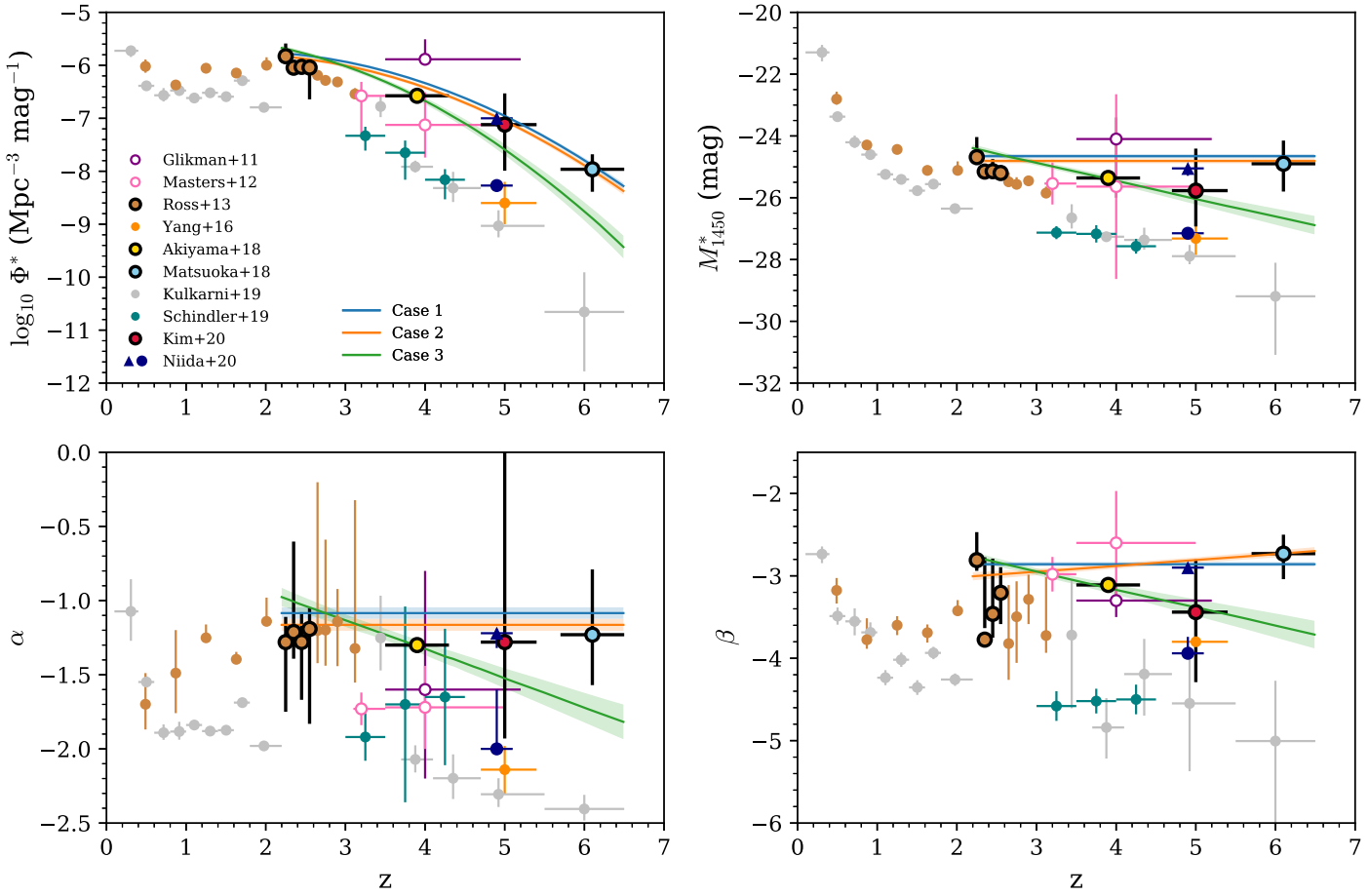

Figure 2. QLF parameters along the redshift. The blue, orange, and green lines represent the best-fit results of cases 1, 2, and 3, respectively, with their 1σ uncertainties (shaded regions). The best-fit parameters from the literature, which are determined without any fixed parameters, are shown as the same symbols in Figure 1, while the data points from the QLFs selected for our model fitting are highlighted by black circles. For Niida et al. (2020), we plot both their results with fixed $\beta = -2.9$ (navy triangles) and without any fixed parameters (navy circles).

QLFs that are not sufficiently constrained due to small number statistics and/or faint-end incompleteness.

Overall, we conclude that, under the current number of data sets, the QLF at $z > 2$ can be well described with a PDE model (case 1) and the addition of the evolution in the other QLF parameters does not improve the fitting result significantly.

The QLF evolution has been studied previously, and several authors deduced the evolution models that are more complicated than the PDE scenario as presented here (Hopkins et al. 2007; Kulkarni et al. 2019). But the high-redshift QLFs in Hopkins et al. (2007) do not extend deep enough to reliably constrain the faint-end QLF shape. Meanwhile, Kulkarni et al. (2019) uses the QLFs down to $M_{1450} \sim -22$ mag at $z \gtrsim 3$, which suffer from a small survey area (Glikman et al. 2011) or a small number of faint quasars (Willott et al. 2010; Kashikawa et al. 2015). We suggest that these are the reason for the discrepancy between the previous results and our result for the QLF evolution. In fact, the most recent work by Shen et al. (2020), including quasars over a wide magnitude range, shows a result in line with our simple PDE models at various redshifts (the gray dashed line in Figure 1). Niida et al. (2020) also suggest little evolution in α and M_{1450} at $4 \lesssim z \lesssim 6$.

4. Simple Model for QLF

The PDE trend of the QLF at $z \gtrsim 2$ is intriguing since, previously, QLFs have been depicted to evolve in a much more complicated way. To explain the universal QLF shape and the PDE behavior, we constructed a theoretically motivated and empirically calibrated QLF model.

Recent observations for individual quasars suggest that there are only small or negligible changes in their intrinsic properties at $2 < z < 6$: the Eddington ratio ($\lambda_{\rm Edd}$) distribution (Mazzucchelli et al. 2017; Kim et al. 2019; Onoue et al. 2019; Shen et al. 2019), the obscured fractions (Vito et al. 2018), the BH-to-galaxy mass ratios (Izumi et al. 2019), and the metal enrichments (Shin et al. 2019; Schindler et al. 2020). This implies that the QLF is not determined by the difference in the characteristics of quasars at $z > 2$, but rather by the characteristics of galaxies/halos in which quasars are embedded. Here, we construct a simple model that is built on a halo mass (M_h) function and several scaling relations to see how such a model can reproduce the observed QLF shape and the PDE behavior.

Starting with the M_h function of Jenkins et al. (2001), we converted this to the stellar mass ($M_{\rm gal}$) function, using the M_h–$M_{\rm gal}$ relation of Behroozi et al. (2019) with a scatter of 0.3–0.025 $\times \log(M_h/10^{10}\,M_\odot)$ dex, inferred from their Figure 12. We used the $z = 2$ relation of all galaxies as a reference, considering the broadly constant shape of their M_h–$M_{\rm gal}$ relation at a redshift range of $2 \leqslant z \leqslant 6$.

Second, the $M_{\rm gal}$ function was converted to the BH mass ($M_{\rm BH}$) function, following the Kormendy & Ho (2013) relation with a scatter of 0.4 dex. Since their relation is given for bulge

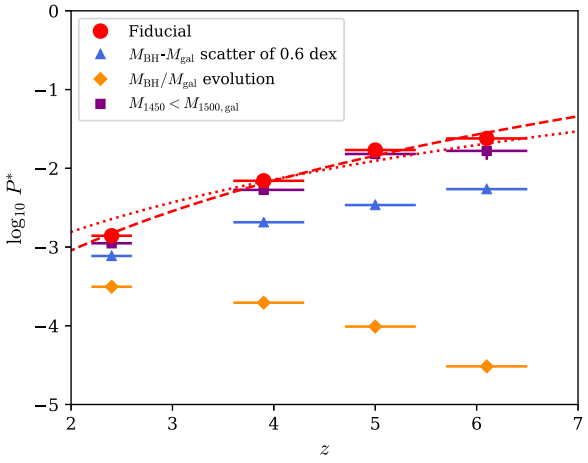

Figure 3. The duty cycle parameter P^* along the redshift. The red circles represent our fiducial model, with P^* changing roughly as $(1+z)^3$ (dotted line) or $(1+z)^4$ (dashed line). The orange diamonds, blue triangles, and purple squares denote the results when including the redshift evolution of M_{BH}/M_{gal}, increasing the scatter in the M_{BH}–M_{gal} relation to 0.6 dex, or adopting a different cut for the outshining effect, respectively.

mass, we used the M_{gal}-dependent bulge-to-total mass ratio, $B/T(M_{gal}) = \min[1,\ 10^{-3.35}M_{gal}^{0.29}]$, derived from a sample of Mendel et al. (2014), giving $M_{BH} \propto M_{gal}^{1.5}$.

Third, the M_{BH} function was converted to the bolometric QLF by convolving it with a log-normal[6] Eddington ratio distribution,

$$P(\lambda_{Edd}) = \frac{P^*}{\sigma\sqrt{2\pi}} \exp\left(\frac{-(\log \lambda_{Edd} - \log \lambda^*_{Edd})^2}{2\sigma^2}\right), \quad (3)$$

where P^* is the normalization factor related to the observable duty cycle related to quasar lifetime and UV obscuration. We set $\log \lambda^*_{Edd} = -0.5$ and $\sigma = 0.3$ dex (Shen et al. 2019). We converted the bolometric luminosity to M_{1450} using the correction factor from Shen et al. (2020).

Lastly, we consider the outshining of AGN in quasar hosts. Previous high-redshift quasar surveys introduced the point-source selection, so it can be assumed that a BH needs to outshine its host galaxy to be selected as a quasar (Ni et al. 2020; Orofino et al. 2021). We classified an AGN as a quasar only when its M_{1450} is twice brighter than the UV magnitude of its galaxy at 1500 Å ($M_{1500,gal}$) inferred from its M_{gal} at a given redshift (Behroozi et al. 2019).

Our QLF model has a number of adjustable parameters, but we allowed only one parameter, P^* in Equation (3), to change its value as a function of redshifts. We scaled P^* to maximize the likelihood function between the model QLF and the selected QLFs at each redshift, and the results are discussed in the following section.

5. Results and Discussion

The resultant P^* values are shown as red circles in Figure 3. Their 1σ errors (68%) were calculated from 100 mock QLFs generated by adding random errors to the Φ_{obs} points. The change in P^* is roughly proportional to $(1+z)^3$ or $(1+z)^4$, shown as the red dotted and dashed lines, respectively. This could be related to the cubic evolution of gas density along the redshift, but we caution that P^* can evolve in a very different way, when some of the model assumptions are modified (see below).

Figure 4 shows that the model QLFs (red solid lines) agree well with the observed ones. Like in the reproduction of galaxy luminosity function from a halo mass function, modeling a QLF from a halo mass function has a tendency of over-producing the number density at low and high luminosity ends. In our model, the faint end of the QLF is suppressed mainly by the outshining effect. If there is no outshining effect, as represented by the red dotted lines in Figure 4, the model would overproduce the faint QSO population. At the bright end, we succeeded in matching the observed QLF by introducing scatters in the scaling relations and the Eddington ratio distribution.

The successful suppression of the QLF faint end via the outshining effect suggests that there may be a large number of faint AGNs ($M_{1450} \gtrsim -24$ mag) that are not identified as quasars due simply to their faintness with respect to host galaxies (the dotted lines in Figure 4). This is also in line with the recent claim on the rapid decrease of AGN fraction among UV sources at that magnitude range (Bowler et al. 2021). Some of the QLFs based on the X-ray detection suggests a large number of faint AGNs, which has been a subject of controversy (Giallongo et al. 2019). The faint AGNs, outshone by their host galaxies in UV (the red dashed lines in Figure 4), may explain such a large number of X-ray faint AGNs by some studies (the green crosses in Figure 4). We also note that the X-ray QLF, converted from our model without the outshining effect using the correction factor from Shen et al. (2020), is roughly consistent with those from the recent X-ray observations at $z \sim 4$ (Aird et al. 2015; Vito et al. 2018). Furthermore, our outshining model suggests that the X-ray QLF does not need to follow the PDE behavior of UV QLF. If this is true and the UV photon escape fraction of the faint AGNs is as high as luminous quasars, the faint AGN population may be responsible for a large fraction of the UV photons required for ionizing the intergalactic medium (Madau & Haardt 2015; Giallongo et al. 2019). For example, our model without outshining effect gives an ionizing emissivity at 912 Å of $\epsilon_{912} \sim 10^{24}$ erg s^{-1} Hz^{-1} Mpc^{-3} at $z = 6$, using Equations (5) and (6) of Kim et al. (2020), which is an order of magnitude higher than the value we would get from the observed QLF (Matsuoka et al. 2018).

Our fiducial model does not include the evolution in the M_{BH}–M_{gal} scaling relation, although several studies support the scaling relation evolution. The scaling relation evolution states that M_{BH} for a given M_{gal} increases as a function of redshift (i.e., the BH grows first, followed by the galaxy growth). Therefore, the quasar luminosity increases for a given M_{gal}, resulting in an overall shift of the model QLF toward higher luminosity, and this is more so at higher redshifts. Additionally, the faint end of QLF increases since the M_{BH}–M_{gal} scaling relation is not linear in our model. If the scaling relation evolves as $\log(M_{BH}/M_{gal}) = 0.28z - 2.91$ (Decarli et al. 2010), however, the mismatch in the faint end is pronounced (the orange dotted lines in Figure 4). Moreover, to match the observed QLF, we need to decrease P^* as a function of redshift (the orange diamonds in Figure 3), which seems contradictory to the expectation that P^* stays constant or increases with redshift.

[6] We also tested the function in the form of the Schechter function, but there is no significant difference in the resultant QLF shape as in Veale et al. (2014). While the physical interpretation could be different, we only considered the light-bulb scenario of quasars for simplicity.

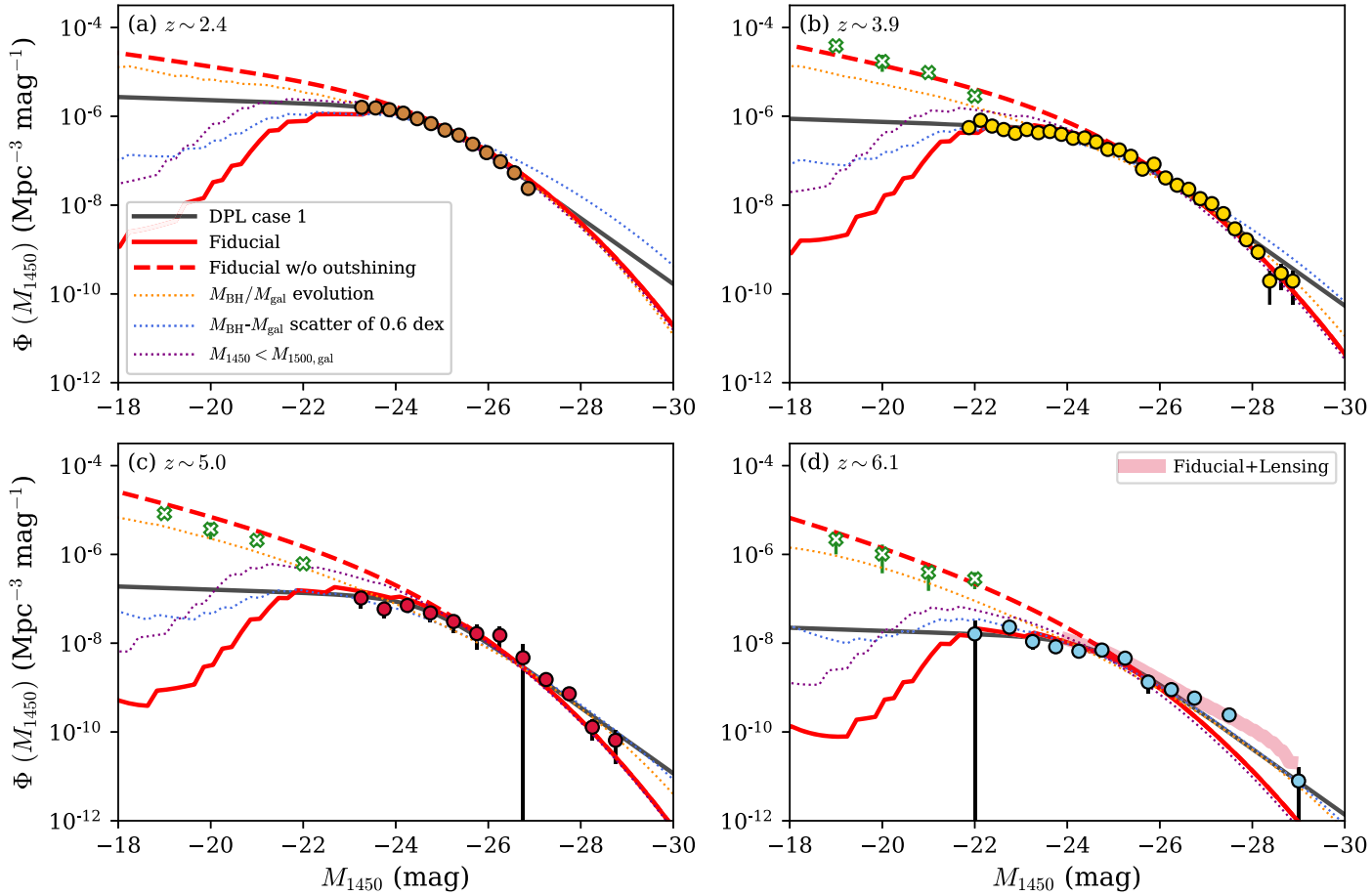

Figure 4. Comparison of the observed QLFs (points), the case 1 QLFs (black lines), and the model QLFs (red lines) at various redshifts. The red solid (dashed) lines represent the model QLF with (without) the outshining effect. The observed QLFs are given by the same symbol as in Figure 1. The orange, blue, and purple dotted lines denote the results with the changes in assumptions, similar to Figure 3. The red translucent line in panel (d) is the expected QLF boosted by the lensing effect assuming the intrinsic QLF slope of $\beta = -3.7$ (Pacucci & Loeb 2020).

The model QLF underpredicts the bright end of the $z = 6$ QLF. One way to cure this problem is to increase the $M_{\rm BH}$–$M_{\rm gal}$ relation scatter to 0.6 dex (the blue dotted lines in Figure 4), which can happen in reality since massive halos are not mandatory for extremely bright/massive quasars (e.g., Di Matteo et al. 2017; Yoon et al. 2019) and outliers from low mass halos can contaminate the bright end easily. However, adopting this assumption overproduces the bright end of lower redshift QLFs. If the $M_{\rm BH}$–$M_{\rm gal}$ relation scatter increases with redshift, such an overproduction can be solved. Another way to solve the bright-end problem of the $z = 6$ model QLF is to introduce the gravitational lensing effect. Our model $z = 6$ QLF has an intrinsic bright-end slope of $\beta \sim -3.7$, and introducing the gravitational lensing effect boosts the QLF shape at the bright end to the observed numbers (the red translucent line in Figure 4, taken from Pacucci & Loeb 2020). For this to be true, a significant fraction of known $z \sim 6$ bright quasars must be lensed, but such lensed bright quasars are still rare (Fan et al. 2019; Fujimoto et al. 2020).

We also explored how the model QLF changes if we adjust the outshining effect criterion. If we loosen the criterion to $M_{1450} < M_{1500,\rm gal}$, to include galaxies with a bit less luminous AGN than our base assumption, the number of quasars increases slightly and mildly at the faint end (the purple line in Figure 4).

6. Conclusion

We investigated the evolution of the UV QLFs at $2 \lesssim z \lesssim 6$ that have been complied from recent large-area surveys. We find that the QLF evolution can be described well with PDE. This result is somewhat unexpected in comparison to the QLF evolution at lower redshifts for which more complicated evolutionary behaviors have been found. Furthermore, we find that the UV QLF at $z > 2$ has a universal DPL function form with a faint-end slope of $\alpha \simeq -1.1$, a break absolute magnitude of $M^*_{1450} \simeq -24.6$ mag, and a bright-end slope of $\beta \simeq -2.9$.

To understand the universal shape of the UV QLF and its PDE, we constructed a model QLF, starting from the M_h function and applying several scaling relations that connect M_h to $M_{\rm gal}$ and $M_{\rm BH}$, and then to quasar luminosity. Additionally, we added the outshining effect of AGN over its host galaxy. With these ingredients, we find that our model QLF can reproduce the observed QLFs at $z > 2$. Although there may be other ways to reproduce the observed QLF behavior, we suggest that the outshining can be an important factor in shaping the UV QLF at high redshift, especially at $z \gtrsim 5$. The importance of the outshining effect implies the existence of many faint AGNs that are buried under the galaxy light, and such faint AGNs could provide a large portion of the UV photons required for ionizing the intergalactic background. Deep and wide NIR spectroscopic surveys with future facilities

could reveal such hidden populations of faint AGN, and allow us to investigate the QLF evolution in a broader context than the simple PDE scenario presented in this work.

We thank the anonymous referee for valuable comments. We thank Linhua Jiang for insightful comments, and Woncheol Jang, Byungwon Kim, and Sungkyu Jung for useful discussion about statistical tests of the QLF evolution. We thank Fabio Pacucci for providing the expected QLF by gravitational lensing effect in Pacucci & Loeb (2020). This work was supported by the National Research Foundation of Korea (NRF) grant (2020R1A2C3011091) funded by the Korean government (MSIP). Y.K. acknowledges the support from the China Postdoc Science General (2020M670022) and Special (2020T130018) Grants funded by the China Postdoctoral Science Foundation.

ORCID iDs

Yongjung Kim https://orcid.org/0000-0003-1647-3286
Myungshin Im https://orcid.org/0000-0002-8537-6714

References

Aird, J., Coil, A. L., Georgakakis, A., et al. 2015, MNRAS, 451, 1892
Akiyama, M., He, W., Ikeda, H., et al. 2018, PASJ, 70, S34
Behroozi, P., Wechsler, R. H., Hearin, A. P., et al. 2019, MNRAS, 488, 3143
Bowler, R. A. A., Adams, N. J., Jarvis, M. J., et al. 2021, MNRAS, 502, 662
Conroy, C., & White, M. 2013, ApJ, 762, 70
Decarli, R., Falomo, R., Treves, A., et al. 2010, MNRAS, 402, 2453
Di Matteo, T., Croft, R. A. C., Feng, Y., et al. 2017, MNRAS, 467, 4243
Fan, X., Wang, F., Yang, J., et al. 2019, ApJL, 870, L11
Foreman-Mackey, D., Hogg, D. W., Lang, D., et al. 2013, PASP, 125, 306
Fujimoto, S., Oguri, M., Nagao, T., et al. 2020, ApJ, 891, 64
Giallongo, E., Grazian, A., Fiore, F., et al. 2019, ApJ, 884, 19
Glikman, E., Djorgovski, S. G., Stern, D., et al. 2011, ApJL, 728, L26
Hopkins, P. F., Richards, G. T., & Hernquist, L. 2007, ApJ, 654, 731
Izumi, T., Onoue, M., Matsuoka, Y., et al. 2019, PASJ, 71, 111
Jenkins, A., Frenk, C. S., White, S. D. M., et al. 2001, MNRAS, 321, 372
Jiang, L., McGreer, I. D., Fan, X., et al. 2016, ApJ, 833, 222
Kashikawa, N., Ishizaki, Y., Willott, C. J., et al. 2015, ApJ, 798, 28
Kim, Y., Im, M., Jeon, Y., et al. 2018, ApJ, 855, 138
Kim, Y., Im, M., Jeon, Y., et al. 2019, ApJ, 870, 86
Kim, Y., Im, M., Jeon, Y., et al. 2020, ApJ, 904, 111
Kormendy, J., & Ho, L. C. 2013, ARA&A, 51, 511
Kulkarni, G., Worseck, G., & Hennawi, J. F. 2019, MNRAS, 488, 1035
Madau, P., & Haardt, F. 2015, ApJL, 813, L8
Manti, S., Gallerani, S., Ferrara, A., Greig, B., & Feruglio, C. 2016, MNRAS, 466, 1160
Masters, D., Capak, P., Salvato, M., et al. 2012, ApJ, 755, 169
Matsuoka, Y., Strauss, M. A., Kashikawa, N., et al. 2018, ApJ, 869, 150
Mazzucchelli, C., Bañados, E., Venemans, B. P., et al. 2017, ApJ, 849, 91
McGreer, I. D., Fan, X., Jiang, L., & Cai, Z. 2018, AJ, 155, 131
Mendel, J. T., Simard, L., Palmer, M., et al. 2014, ApJS, 210, 3
Ni, Y., Di Matteo, T., Gilli, R., et al. 2020, MNRAS, 495, 2135
Niida, M., Nagao, T., Ikeda, H., et al. 2020, ApJ, 904, 89
Onoue, M., Kashikawa, N., Matsuoka, Y., et al. 2019, ApJ, 880, 77
Orofino, M. C., Ferrara, A., & Gallerani, S. 2021, MNRAS, 502, 2757
Pacucci, F., & Loeb, A. 2020, ApJ, 889, 52
Palanque-Delabrouille, N., Magneville, C., Yèche, C., et al. 2016, A&A, 587, A41
Ren, K., Trenti, M., & Di Matteo, T. 2020, ApJ, 894, 124
Ross, N. P., McGreer, I. D., White, M., et al. 2013, ApJ, 773, 14
Schindler, J.-T., Fan, X., McGreer, I. D., et al. 2019, ApJ, 871, 258
Schindler, J.-T., Farina, E. P., Bañados, E., et al. 2020, ApJ, 905, 51
Shen, X., Hopkins, P. F., Faucher-Giguère, C.-A., et al. 2020, MNRAS, 495, 3252
Shen, Y., Wu, J., Jiang, L., et al. 2019, ApJ, 873, 35
Shin, J., Nagao, T., Woo, J.-H., et al. 2019, ApJ, 874, 22
Shin, S., Im, M., Kim, Y., et al. 2020, ApJ, 893, 45
Tucci, M., & Volonteri, M. 2017, A&A, 600, A64
Veale, M., White, M., & Conroy, C. 2014, MNRAS, 445, 1144
Vito, F., Brandt, W. N., Yang, G., et al. 2018, MNRAS, 473, 2378
Willott, C. J., Delorme, P., Reylé, C., et al. 2010, AJ, 139, 906
Wyithe, J. S. B., & Loeb, A. 2002, ApJ, 577, 57
Yang, J., Wang, F., Wu, X.-B., et al. 2016, ApJ, 829, 33
Yoon, Y., Im, M., Hyun, M., et al. 2019, ApJ, 871, 57